Nanoelectronics and Its New Materials – A NEW ERA OF NANOSCIENCE

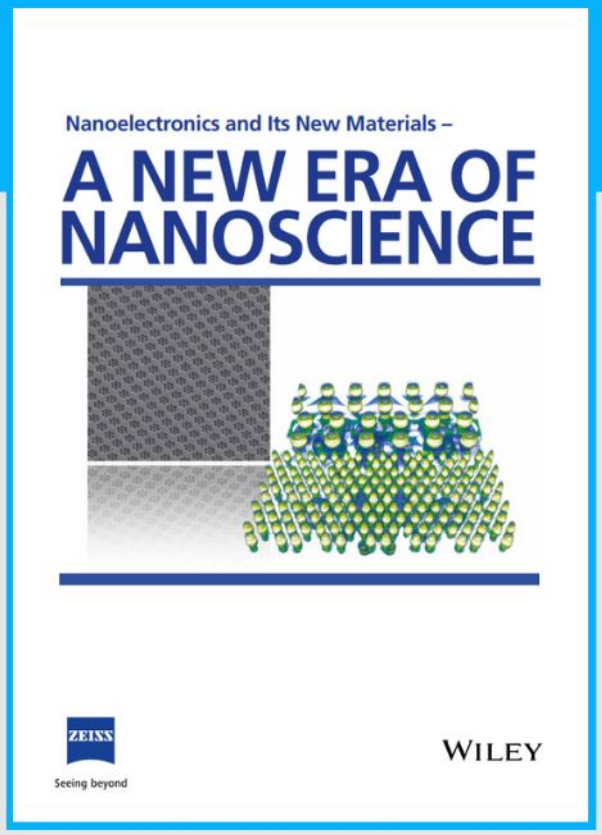

Discover the recent advances in electronics research and fundamental nanoscience.

Nanotechnology has become the driving force behind breakthroughs in engineering, materials science, physics, chemistry, and biological sciences. In this compendium, we delve into a wide range of novel applications that highlight recent advances in electronics research and fundamental nanoscience. From surface analysis and defect detection to tailored optical functionality and transparent nanowire electrodes, this eBook covers key topics that will revolutionize the future of electronics.

To get your hands on this valuable resource and unleash the power of nanotechnology, simply download the eBook now. Stay ahead of the curve and embrace the future of electronics with nanoscience as your guide.

ZEISS

Seeing beyond

WILEY

NANO · MICRO small
www.small-journal.com

Soft Phonon Mode Triggering Fast Ag Diffusion in Superionic Argyrodite Ag_8GeSe_6

Xingchen Shen, Michael Marek Koza, Yung-Hsiang Tung, Niuchang Ouyang, Chun-Chuen Yang, Chen Wang, Yue Chen, Kristin Willa, Rolf Heid, Xiaoyuan Zhou,* and Frank Weber**

The structural coexistence of dual rigid and mobile sublattices in superionic Argyrodites yields ultralow lattice thermal conductivity along with decent electrical and ionic conductivities and therefore attracts intense interest for batteries, fuel cells, and thermoelectric applications. However, a comprehensive understanding of their underlying lattice and diffusive dynamics in terms of the interplay between phonons and mobile ions is missing. Herein, inelastic neutron scattering is employed to unravel that phonon softening on heating to $T_c \approx 350$ K triggers fast Ag diffusion in the canonical superionic Argyrodite Ag_8GeSe_6. Ab initio molecular dynamics simulations reproduce the experimental neutron scattering signals and identify the partially ultrafast Ag diffusion with a large diffusion coefficient of 10^{-4} cm^{-2} s^{-1}. The study illustrates the microscopic interconnection between soft phonons and mobile ions and provides a paradigm for an intertwined interaction of the lattice and diffusive dynamics in superionic materials.

1. Introduction

Tailoring thermal conductivity κ is at the core of various modern microelectronic and energy conversion devices.[1] A high κ is indispensable for electronic circuit substrates and thermal interfaces to enable efficient heat dissipation from thermal hot spots.[1b] In contrast, a low κ is desired to minimize heat transport in thermoelectric materials (TEMs),[1c,d] thermal insulators,[1e] and thermal barrier coatings.[1f] In principle, the total thermal conductivity of a solid consists of contributions from the various excitations, such as electrical carriers (holes or electrons), lattice vibrations (phonons), electromagnetic waves, and spin excitations. For electronic reasons best-performing TEMs are semiconductors and semimetallic compounds, and their overall thermal conductivity is hence dominated by the lattice thermal conductivity κ_L. Therefore, the phonon contribution to the heat transport has to be reduced to optimize thermoelectric performance of materials.

Different mechanisms and strategies are employed to minimize κ_L in TEMs.[2] In general, structural complexity reduces

X. Shen, K. Willa, R. Heid, F. Weber
Institute for Quantum Materials and Technologies
Karlsruhe Institute of Technology
76021 Karlsruhe, Germany
E-mail: xingchen.shen@ensicaen.fr; Frank.weber@kit.edu

X. Shen, X. Zhou
College of Physics and Center of Quantum Materials and Devices
Chongqing University
Chongqing 401331, P. R. China
E-mail: xiaoyuan2013@cqu.edu.cn

X. Shen
Laboratoire de Cristallographie et Sciences des Matériaux (CRISMAT)
CNRS
ENSICAEN
Caen 14000, France

The ORCID identification number(s) for the author(s) of this article can be found under https://doi.org/10.1002/smll.202305048

DOI: 10.1002/smll.202305048

M. M. Koza
Institute Laue Langevin
6 Rue Jules Horowitz, B.P. 156, Grenoble, Cedex 9 38042, France

Y.-H. Tung
Department of Physics
National Yat-sen University
Kaohsiung 80424, Taiwan

Y.-H. Tung
Jülich Centre for Neutron Science JCNS at Maier-Leibnitz Zentrum (MLZ)
Forschungszentrum Jülich GmbH
Lichtenbergstraße 1, D-85747 Garching, Germany

N. Ouyang, C. Wang, Y. Chen
Department of Mechanical Engineering
The University of Hong Kong
Pokfulam Road, Hong Kong, SAR China

C.-C. Yang
Department of Physics
National Central University
Chung-Li District, Taoyuan City 32001, Taiwan

C.-C. Yang
Department of Physics
Chun Yuan Christian University
Chung-Li District, Taoyuan City 32023, Taiwan

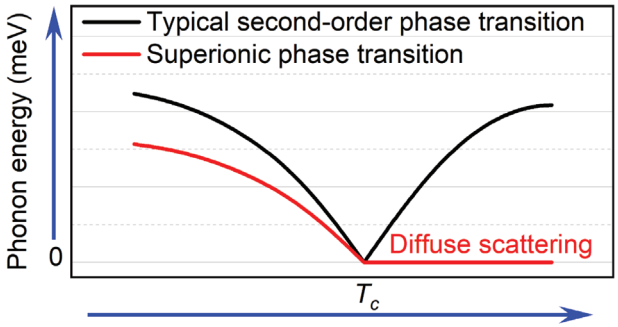

Figure 1. (Black solid line) Schematic diagram of the temperature dependence of the energy of a typical soft phonon in a second-order phase transition, such as a ferroelectric one. (Red solid line) Soft phonon behavior observed in Ag_8GeSe_6 undergoing a superionic phase transition upon heating.

the relative number of propagating acoustic and thus heat carrying excitations. The formation of low-energy and strongly localized optical phonon modes by alloying with heavy elements expands the phase space of phonon–phonon Umklapp scattering processes. A pronounced anharmonicity arising from weak chemical bonding enhances the probability of phonon–phonon scattering events. A particular mechanism and prominent source of lattice anharmonicity is the effect of soft phonon mode, such as in the vicinity of structural phase transitions.[3]

A continuous structural phase transition is accompanied by a soft phonon mode, i.e., a normal collective mode that features an anomalous decrease of its frequency to zero when approaching the phase transition temperature T_c.[4] In the context of the Landau theory and anharmonic interactions proposed by Cochran, mean-field theory describes the temperature-dependent soft phonon mode energy ω_s as[4]

$$\omega_s^2\ (q_s, j) = A\left|T - T_C\right| \quad (1)$$

where q_s and j are the wave vector of the soft mode and its branch index, respectively. A is a material-specific constant and T is the absolute temperature. This temperature response is sketched in **Figure 1**. The model predicts that a specific phonon of the high symmetry phase softens progressively approaching the phase transition temperature T_c. The phonon energy reaches zero and its displacement pattern freezes into a static lattice distortion at T_c. In the distorted phase, the phonon energy hardens again and corresponds to an optic mode at the zone center. This soft mode scenario has been verified in many materials, where the prototypical ferroelectric $SrTiO_3$ was among the first.[5]

However, here we study the case of a superionic phase transition in the Argyrodite Ag_8GeSe_6, where the soft mode does not freeze into a static distortion but rather triggers solid state diffusion upon crossing T_c. Consistently, no phonon hardening is observed in the superionic phase above T_c and the soft mode maintains its over-damped character as indicated in Figure 1. This duality of lattice and diffusive dynamics in the superionic phase is responsible for intriguing thermal transport properties, and provokes interest for applications in rechargeable batteries,[6] fuel cells,[7] and especially thermoelectrics.[8]

Besides the well-known canonical superionic conductors $(Cu, Ag)_2Se$[9] and (Ag, Cu)$CrSe_2$,[10] Cu- and Ag-based Argyrodites, such as Ag_9GaSe_6,[11] Ag_8SnSe_6,[12] and Cu_7PSe_6,[13] have recently attracted considerable interest as potential TEMs,[14] as they show a T-independent and ultralow κ_L of ≈0.3 W m^{-1} K^{-1}.[8b] Argyrodites contain an enormous abundance of chemical compositions with the general formula of $A^+_m\ B^{n+}{}_{(12-n)/m}\ X^{2-}{}_6$ (A^+ = Li^+, Cu^+, Ag^+, B^{n+} = Al^{3+}, Ga^{3+}, Si^{4+}, Ge^{4+}, Sn^{4+}, P^{5+}, As^{5+}, and X^{2-} = S^{2-}, Se^{2-}, Te^{2-}). They undergo multiple phase transitions toward a high-temperature superionic face-centered cubic structure,[15] yielding rich physical and chemical material properties. Their atomic lattice consists of two sets of independent sublattices formed, on one hand, by a rigid framework of tetrahedrally coordinated $[BX4]^{(8-x)-}$ polyanions attached to X^{2-} anions and, on the other, by weakly bonded A^+ cations.[15,16] It is these weakly bonded A^+ cations, which can continuously hop into the adjacent vacant sites in the superionic phase forming a mobile sublattice in the framework of the rigid sublattice.

So far, Ag-based Argyrodites have been extensively studied for their macroscopic thermal transport properties. Investigations of their complex phase transitions behavior, and intriguing lattice dynamics properties as well as diffusive mechanisms remain sparse. Herein, we report results from inelastic neutron scattering (INS) and quasielastic neutron scattering (QENS) as well as synchrotron X-ray diffraction (SYXRD) and ab initio molecular dynamics (AIMD) on the representative silver-based Argyrodite Ag_8GeSe_6. Our SYXRD results identify the multiple phase transitions and provide a map view of the Ag atomic diffusion pathway. The INS results uncover phonon softening yielding fast Ag diffusion approaching T_c, which originates from low-lying Ag-dominated phonons. We elucidate a maintained over-damped soft phonon mode in the superionic phase and a prominent QENS signal as a footprint of an extraordinarily high Ag mobility. We approximate from AIMD results the experimental INS and QENS signals, and elaborate the fast Ag diffusion behavior in Ag_8GeSe_6.

2. Results and Discussion

2.1. Multiple Phase Transitions and Crystal Structures

In a previous work,[17] some of us reported on the high-temperature crystal structures of Ag_8GeSe_6 observed via lab-based X-ray difftraction (XRD) and specific heat measurements. The study disclosed an inconsistency in the number of phase transitions. Our XRD data identified a single-phase transition from a room-temperature orthorhombic phase ($Pmn2_1$) to a high-temperature cubic phase (F-$43m$). Whereas several phase transitions were revealed through endothermic peaks in the heat capacity measurements in an equivalent temperature range. To solve this apparent discrepancy, we performed high-resolution SYXRD in an extended temperature range from 250 to 600 K and complemented the structural study by heat capacity data toward very low temperatures. The results of this experiment are compiled in **Figure 2**a–c and Rietveld refinements of the SYXRD data are reported in Figure S1a–d of the Supporting Information section.

The present SYXRD results reveal phase transitions at T = 269, 317, and 350 K and thus confirm that Ag_8GeSe_6 adopts an orthorhombic structure at room temperature and a cubic

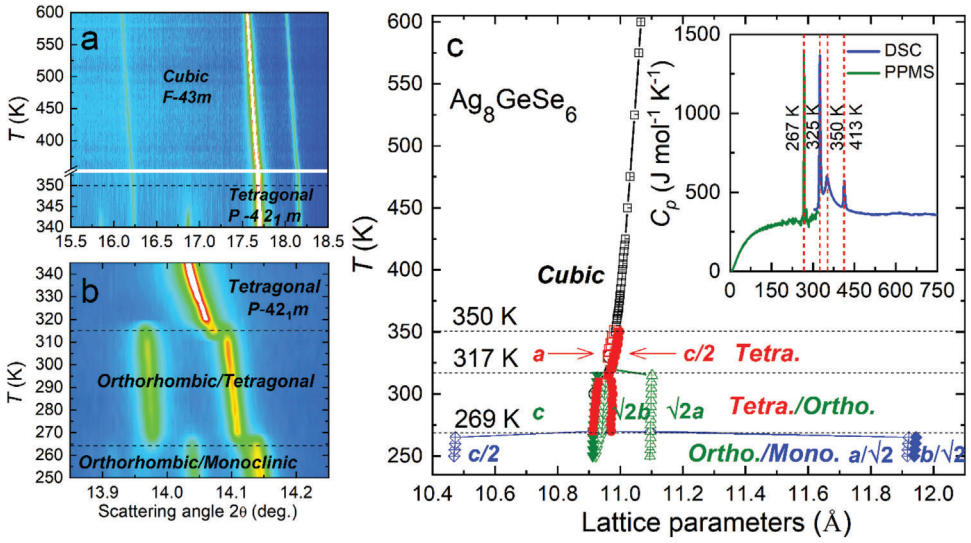

Figure 2. a,b) Contour plots of the temperature evolution of SYXRD of a Ag_8GeSe_6 powder sample. c) Corresponding temperature-dependent lattice parameters deduced by Rietveld fitting. (Inset) Heat capacity measurements of Ag_8GeSe_6 (green and blue solid lines). Phase transition temperatures are specified in the plot (vertical red dashed lines).

phase above 350 K. Endothermic peaks observed in the heat capacity measurements (inset in Figure 2c) are in line with these findings. However, specific heat indicates an additional transition at 413 K, which is undetected by SYXRD. This additional transition might be associated with changes in the local structure of Ag ions and requires further investigations which are beyond the scope of the current report. The sequence of phase transitions is indicated in Figure 2c along with the refined lattice parameters of the respective phases. We conclude from Rietveld refinements that the orthorhombic phase coexists as a major fraction with a monoclinic structure (*P112*, 8%) below 265 K, and with a tetragonal phase (*P-42$_1$m*, 2.5%) in the temperature regime 270–315 K (Figure S1e, Supporting Information). Ag_8GeSe_6 forms a single tetragonal phase from 320 to 350 K and ultimately enters into a single superionic cubic phase (*F-43m*) above 350 K as indicated in Figure 2c.

2.2. Ag Diffusion Pathway

Our SYXRD analysis shows that high-*T* cubic phase of Ag_8GeSe_6 consists of structural motives formed on one hand by Se and Ge, and by Ag on the other displayed in **Figure 3**a. Se occupies fcc positions and forms with Ge tetrahedral $GeSe_4$ units located at the mid-points of the fcc cell edges. The crystal symmetry allows the Ag cations to be located on three different sites Ag1-Ag3 leading to their random partial occupation, and thus structural disorder and extensive free space in the Ag sublattice. This partially-filled sublattice features a channel network for Ag diffusion. To explicitly visualize the Ag diffusion channels in the superionic phase, we show the 2D electron-density maps (EDMs) deduced from Rietveld refinements in Figure 3b. The *T*-dependent 2D-EDMs in the (1 1 −1) plane display well-defined spots for Ag atoms at $T < 350$ K. At 350 and 600 K, we note progressive overlap of the electron density between Ag2-Ag1-Ag2 positions best seen in the (1 1-1) plane, which implies that Ag1 and Ag2 sites are interconnected and form effective diffusion channels. The *T*-dependent EDMs verify that the Ag atoms become strongly delocalized and diffuse into unoccupied lattice sites on entering the high-temperature cubic phase at $T_c \approx 350$ K.

2.3. Phonon Softening and Quasielastic Neutron Scattering

Phonons are the main heat carriers in Ag_8GeSe_6 and responsible for the reported[17] ultralow lattice thermal conductivity of ≈0.3–0.4 W m^{-1} K^{-1}. Therefore, we performed neutron spectroscopy measurements to investigate the lattice dynamics properties. The experiments were performed on the thermal neutron time-of-flight spectrometer PANTHER located at the European Neutron Source Institut Laue Langevin in Grenoble, France. A wide range of temperatures from 2 to 600 K was exploited with three incident energies $E_i = 12.5$, 30, and 50 meV. This allows to analyze the full Phonon density of states (PDOS) of the different phases as well as the diffuse scattering close to zero energy transfer in search of fingerprints of the diffusion processes. Here, we focus only on the results obtained with the best energy resolution using $E_i = 12.5$ meV. The analysis of data with higher incident energies is shown in Figures S2, S3, and Note S1 (Supporting Information). We note that AIMD simulations, which we also use below to investigate the neutron scattering intensities and diffuse scattering, are in good agreement with the PDOS deduced from our experimental data.

Contour maps of neutron scattering intensity, the dynamic structure factor $S(|\boldsymbol{Q}|, E)$, are shown in **Figure 4**a–c for various temperatures below and above the superionic phase transition temperature T_c. Most prominently, we observe the signature of a Ag-dominated (see Figures S3, S4, and Note S1 in the Supporting Information) low-lying optic phonon mode of 3 meV at room temperature (white arrow in Figure 4a) which cannot be distinguished anymore from the elastic scattering at higher temperatures (Figure 4b,c). We investigated the behavior of this

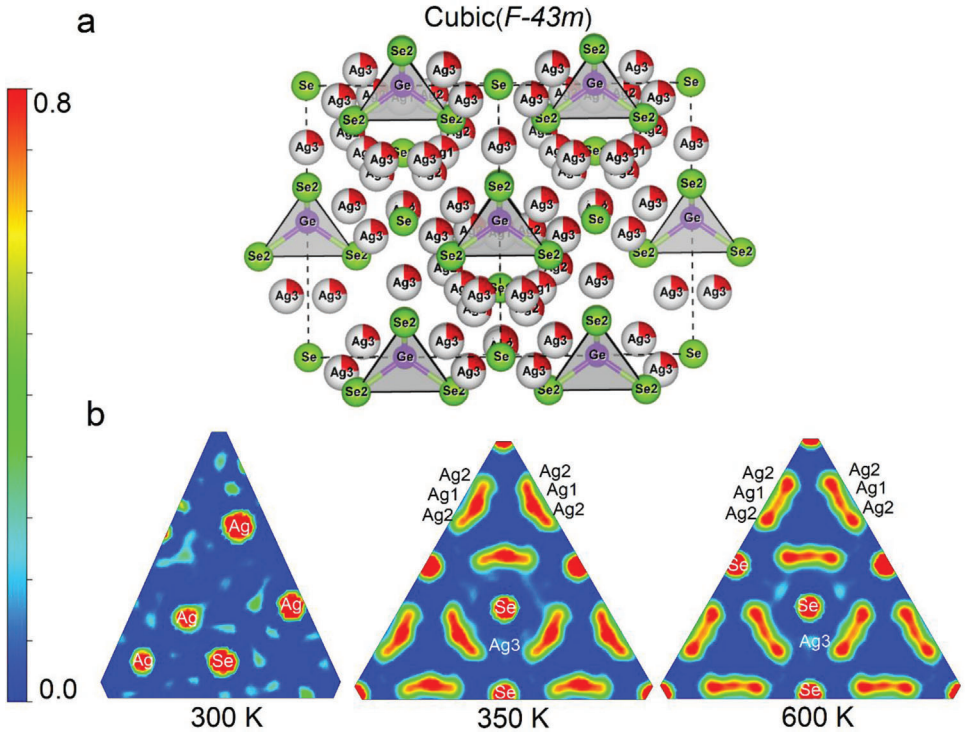

Figure 3. a) Crystal structure of Ag_8GeSe_6 in the high-temperature cubic phase (*F-43m*). Allowed Ag positions are shown with their partial site occupancy (red/gray), while Ge and Se atoms are shown in purple and green, respectively. b) 2D electron density maps at 300, 350, and 600 K in (1 1 −1) planes. Lattice vectors in (b) refer to the respective out-of-plane directions.

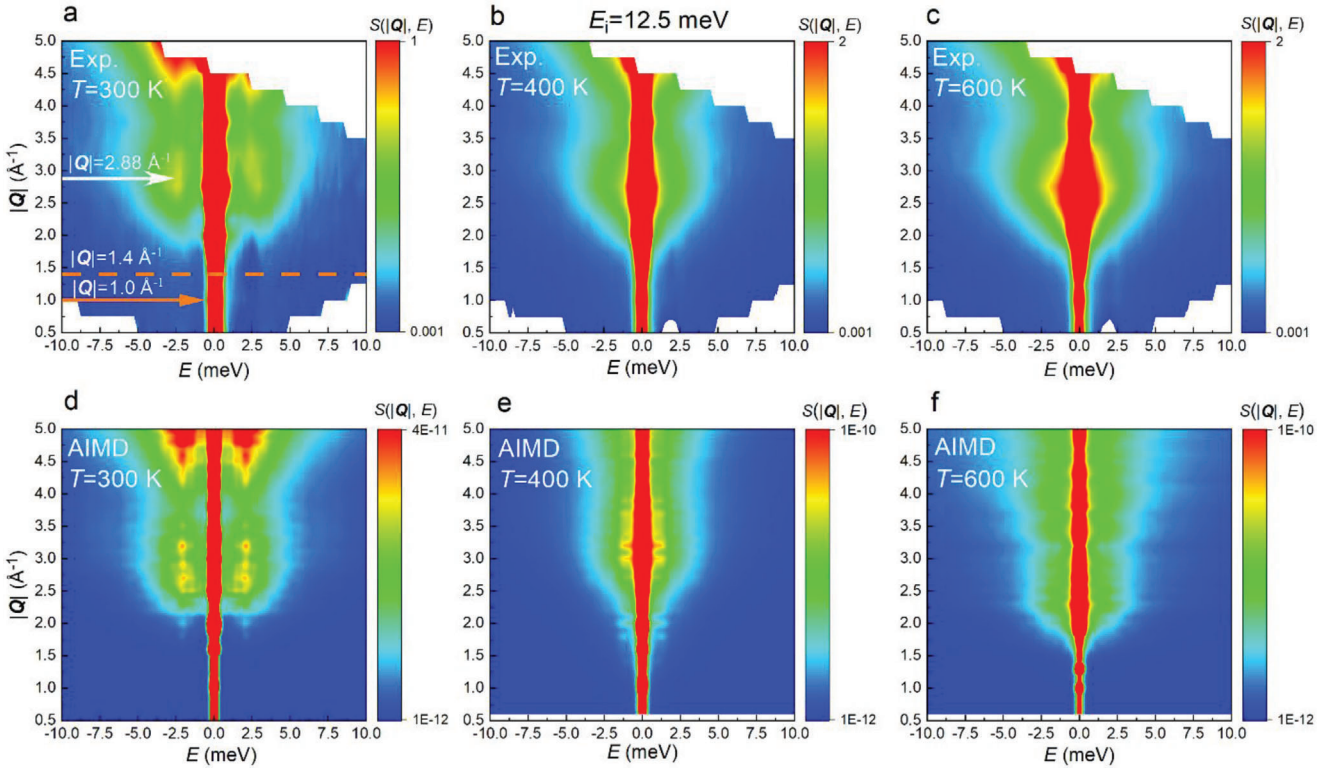

Figure 4. a–c) Experimental $S(|\boldsymbol{Q}|, E)$ at $T = 300$, 400, and 600 K, respectively. d–f) Simulated $S(|\boldsymbol{Q}|,E)$ based on AIMD computed for corresponding T. White and orange vertical arrows and dash orange line in (a) denote characteristic wave vectors $|\boldsymbol{Q}|$ exploited in our analysis of the soft phonon mode (see Figure 5) and the diffusive motion of Ag (see Figure 6).

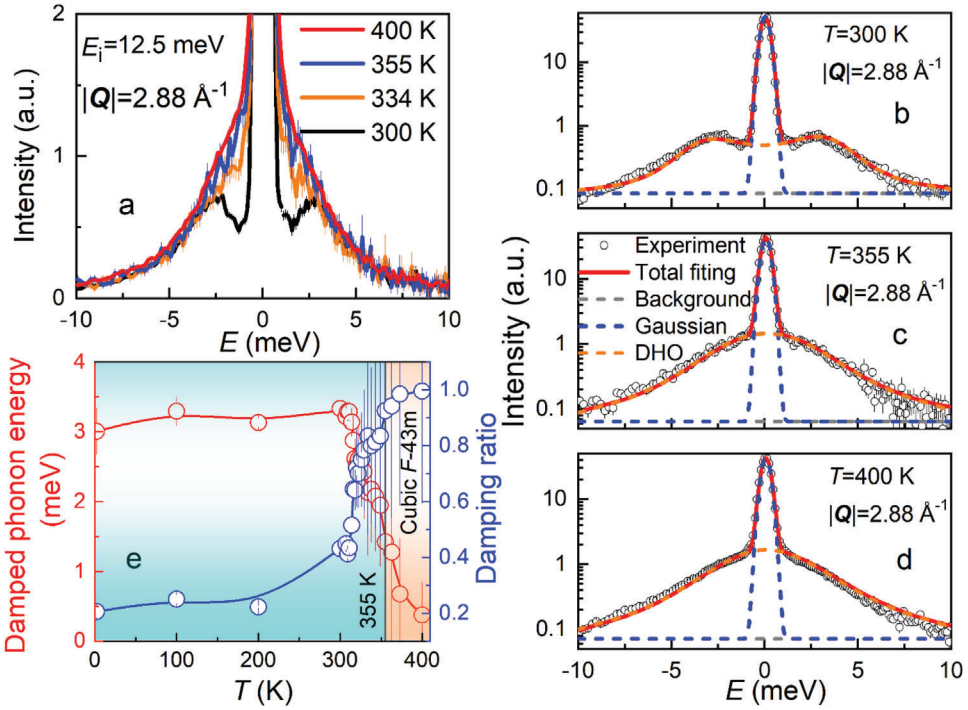

Figure 5. a) Measured $S(|\boldsymbol{Q}|, E)$ at $|\boldsymbol{Q}| = (2.88 \pm 0.125)$ Å^{-1} at $T = 300$, 334, 355, and 400 K. b–d) Same data sets (open black circles) with the fitting profiles approximating the soft phonon mode (DHO) and elastic contribution (Gaussian). e) Temperature dependence of the damped soft-phonon energy and damping ratio from 2 to 400 K.

distinct phonon signal analyzing constant-momentum spectra at $|\boldsymbol{Q}| = (2.88 \pm 0.125)$ Å^{-1}, where this signal is best visible. The constant $|\boldsymbol{Q}|$ spectra (**Figure 5**a; and Figure S5, Supporting Information) were modeled by approximating the phonon signal with a damped harmonic oscillator (DHO) function[18] and the elastic line with a delta function both convoluted with a Gaussian-shaped resolution of 0.6 meV full-width at half-maximum (FWHM) (Figure 5b–d). The derived characteristic energy of the DHO reveals a continuous softening of the phonon peak above 300 K (Figure 5e). This softening continues up to the transition temperature T_c at which the phonon peak becomes overdamped evidenced also by the damping ratio (Figure 5e) and its characteristic energy is indistinguishable from zero energy. Interestingly, upon further heating the phonon does not recover a finite energy value as expected for a 2nd order phase transition outlined above.[4]

On the contrary, the overdamped DHO signal develops into a persistent QENS signal well-visible at all temperatures in the superionic phase. A QENS signal is the footprint of enhanced structural relaxation, such as a translational diffusion process. In summary, Ag_8GeSe_6 is characterized by a phonon softening on heating toward the superionic phase transition. This soft phonon turns into a temperature-independent overdamped phonon above the phase transition where mass transport becomes apparent. This is in contrast to other continuous structural phase transitions featuring a soft phonon mode, such as antiferrodistortive transitions in ferroelectric[4a,19] or charge-density-wave transitions,[20] where the soft mode recovers finite energies both above and below the transition temperatures.

To obtain deeper insight into the vibrational and diffusive properties of Ag_8GeSe_6, we employ AIMD calculations to simulate the experimental signals. This is in particular important as the experimentally monitored neutron scattering response consists of coherent and incoherent contributions whereby in Ag_8GeSe_6 it is dominated by the coherent scattering and, specifically at low energies, by the coherent response of the Ag atoms. The low-temperature crystal structure can currently not be assessed by the applied AIMD method since the large unit cell is beyond our computational limits as outlined in the Experimental Section. As for the room- and higher-temperature phases, the good agreement with the measured PDOS (see Figure S3, Supporting Information) indicates that the lattice dynamics are well-captured by our AIMD simulations. Here, we focus on the low-energy transfers/processes visible in our high-resolution INS measurements (Figure 4a–c). We use the MDANSE[21] software package to simulate the corresponding neutron scattering intensities based on the AIMD simulations and find close resemblance between theory (Figure 4d–f) and experiment (Figure 4a–c). We highlight in particular the matching optic phonon mode at 3 meV at 300 K (white arrow in Figure 4a,d) and the broad QENS intensities at higher temperatures (Figure 4b,c,e,f).

2.3. Experimental and Simulated Constant Momentum Inelastic Intensities

Diffuse scattering can be best studied at low $|\boldsymbol{Q}|$ where phonons are hardly detectable due to their $\boldsymbol{Q}^2$-dependent structure

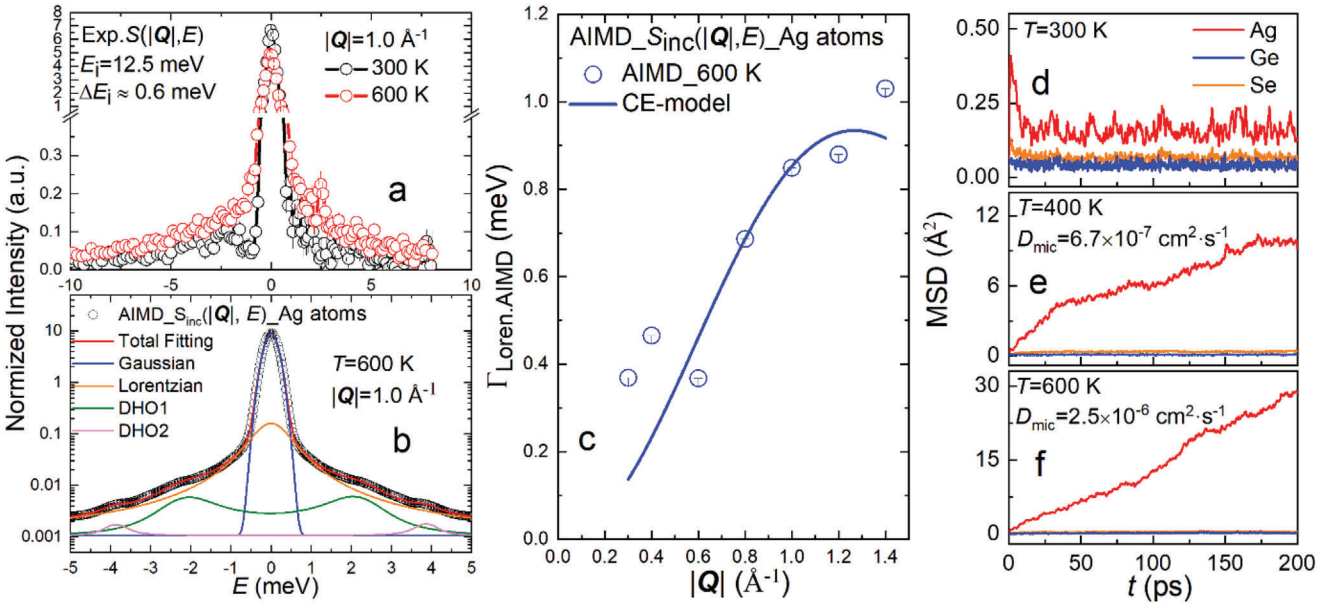

Figure 6. a) Measured $S(|\boldsymbol{Q}|, E)$ with results from QENS fits at $|\boldsymbol{Q}| = (1.0 \pm 0.125)$ Å^{-1} at 300 and 600 K. b) AIMD simulated incoherent $S_{inc}(|\boldsymbol{Q}|, E)$ with QENS fit results. AIMD data are represented by open black circles, total QENS fit results by red solid lines. The fit components of a Gaussian, Lorentzian, and two DHO functions are indicated by blue, orange, green, and pink dashed lines, respectively. The Lorentz function was convoluted with the Gaussian-like resolution function. c) Lorentzian Γ derived from the fits of the incoherent signal (open circles) at 600 K. Solid lines represent fits of the Chudley–Elliot model of jump-diffusion to the data. Atomic mean-square displacement (MSD) computed from AIMD at d) 300 K, e) 400 K, and f) 600 K. The red, blue, and orange solid lines denote Ag, Ge, and Se atoms, respectively.

factors. Our data show that phonon intensities start to rise for momenta larger than 1.5 Å^{-1} (Figure 4a–c). Hence, we extract data based on a smaller $|\boldsymbol{Q}|$ and analyze atomic diffusion by analyzing the experimental $S(|\boldsymbol{Q}|, E)$ over the $|\boldsymbol{Q}|$ range of (0.8, 1.4 Å^{-1}). At room temperature the data show a resolution limited Gaussian-shaped elastic contribution and an essentially featureless inelastic regime (see black solid line in **Figure 6**a). All spectra in the supersonic phase ($T > T_c$ = 350 K) exhibit an essential resolution function and an additional Lorentzian contribution centered at zero energy (e.g., red line at 600 K in Figure 6a) accounting for the observed QENS signal.

To shed light on the individual dynamics of the Ag atoms, we compute from the AIMD data the purely incoherent scattering signal. As highlighted in Figure 6b the $S_{inc,AIMD}(|\boldsymbol{Q}|, E)$ of Ag was approximated by an elastic contribution, two DHO functions accounting for residual phonon signals, and a Lorentz function for the diffusive signal centered around zero energy at 600 K. The Lorentz function as well as the elastic line took account of a Gaussian-shaped resolution with FWHM = 0.38 meV which resulted from the computation of the $S_{inc,AIMD}(|\boldsymbol{Q}|, E)$. The FWHM = 0.38 meV of the resolution function was chosen because it was the higher limit value of our AIMD simulations. The $S_{inc}(|\boldsymbol{Q}|, E)$ is the Fourier transform of the self-correlation function of Ag comprehending information on the speed and geometry of a potential diffusion mechanism. For translational relaxations in solid state matter a widely used concept is the jump-diffusion model by Chudley and Elliot (CE).[22] It is built upon the assumption that atoms execute jumps with an averaged finite length d between some lattice sites at which they are locked for a residence time τ between consecutive jumps. The CE model anticipates a $|\boldsymbol{Q}|$-dependent broadening of a Lorentzian-shaped $S_{inc}(|\boldsymbol{Q}|, E)$ response as

$$\Gamma_{\text{Lor, AIMD}}\left(|\mathbf{Q}|\right) = \frac{2\hbar}{\tau}\left(1 - \frac{\sin\left(|\mathbf{Q}|\, d\right)}{\left(|\mathbf{Q}|\, d\right)}\right) \tag{2}$$

with the Planck constant $\hbar$. The parameters can be related to a microscopic diffusion coefficients D_{mic} as

$$D_{\text{mic}} = \frac{d^2}{6\tau} \tag{3}$$

In view of the afore presented SYXRD results, it is appropriate for the present relaxation case as it was successfully used for the analysis of diffusion processes in other solid-state compounds.[23] Selected spectra at 600 K with fitted profiles are shown in Figure 6b and the approximated $\Gamma_{Lor,AIMD}$ are reported in Figure 6c. At 600 K the CE model yields a short residence time of 1.7(1) ps, a large average jump distance of 3.5(2) Å and a large diffusion coefficient $D_{mic} \approx 1.23 \times 10^{-4}$ cm^{-2} s^{-1}, indicating ultrafast diffusion dynamics in the superionic phase of Ag_8GeSe_6.

In contrast to the $S_{inc,AIMD}(|\boldsymbol{Q}|, E)$ analysis the computation of diffusion parameters from mean square displacement (MSD) of the atoms comprises processes on length and time scales of the box size and period of simulation, respectively. In Figure 6d–f, we highlight that the MSDs disclose the Se and Ge atoms as being immobile at any temperature and time of the simulation. This holds as well for MSD of Ag at 300 K. However, from 400 K on, the MSDs of Ag give evidence of a temperature-activated process. Approximating the MSD with a linear fit yields the macroscopic diffusion coefficients $D_{mac} \approx 6.70 \times 10^{-7}$ cm^{-2} s^{-1} at 400 K,

Table 1. Temperature-dependent diffusion parameters of Ag atoms based on AIMD data. D_{mac} are calculated from Ag mean-square displacements.

T [K]	D_{mac} [10^{-6} cm^{-2} s^{-1}]
400	0.67(6)
500	1.7(3)
600	2.5(2)

1.70×10^{-6} cm^{-2} s^{-1} at 500 K, and 2.50×10^{-6} cm^{-2} s^{-1} at 600 K (**Table 1**), implying a slower diffusion of Ag on the macroscopic length and time scales. Our combined experimental and theoretical results suggest that multiple diffusion processes of a wide range of time and length scales are present in Ag_8GeSe_6.

3. Conclusion

We implement a comprehensive study on lattice and diffusion dynamics and elaborate on the interconnection between soft phonons and mobile ions in superionic Argyrodites. Our AIMD analysis indicates that the investigated Argyrodites Ag_8GeSe_6 feature partially fast Ag diffusion expressed in a microscopically diffusion coefficient $D_{mic} \approx 10^{-4}$ cm^{-2} s^{-1} at 600 K, which is higher than that of other reported superionic thermoelectric materials, such as Cu_2Se[23a] ($D \approx 10^{-5}$–10^{-7} cm^{-2} s^{-1} over 500–700 K), $AgCrSe_2$[23b] ($D \approx 1.5 \times 10^{-5}$ cm^{-2} s^{-1}at 600 K), $CuCrSe_2$[23c] (7.2×10^{-6} cm^{-2} s^{-1} at 495 K), and Cu_7PSe_6[23e] ($D \approx 2.31 \times 10^{-5}$ cm^{-2} s^{-1} at 500 K). This rapid diffusion is in line with our INS data indicating a visible QENS signal in the superionic state of Ag_8GeSe_6. However, beyond this exceptionally high D_{mic} an analysis of the AIMD-derived MSD of Ag gives evidence of a coexistence of slower diffusion processes on macroscopic length and time scales. With a computed $D_{mac} \approx 10^{-6}$ cm^{-2} s^{-1} for temperatures in the superionic state the AIMD data point at a rich multiplicity and complexity of Ag diffusion processes. As consequence of the large variation of diffusion coefficients in terms of microscopic and macroscopic time scales, further experimental investigations and customized theoretical modeling are required to quantify the Ag diffusion dynamics.

The aforementioned INS studies of diffusion processes in different superionic TEMs utilized cold neutron time-of-flight techniques with an energy resolution of ≈0.1–0.3 meV. In this study, we used thermal neutron time-of-flight spectroscopy with an energy resolution of ≈0.6 meV to shed light on vibrational and relaxational properties in an excessive temperature range from the ground state up to the superionic phase of Ag_8GeSe_6. In the presence of relaxational scenarios as rich as those observed in the superionic TEMs, varying experimental conditions with cold and thermal neutrons might have a filter effect on the diffusion process detected. The high resolution but reduced dynamic range of cold neutrons make them more sensitive to slower processes than thermal neutrons offering a wide dynamic range at a moderate resolution.

Most prominently, our temperature-dependent experiments and calculations reveal that phonon softening precedes and triggers fast Ag diffusion in the superionic phase in Ag_8GeSe_6. The damped Ag-dominated soft phonon transforms into Ag diffuse scattering upon entering the superionic state, which is different from the typically observed hardening of a soft phonon below as well as above a second-order phase transition. Apart from this distinctly unique over-damped soft phonon inducing Ag diffusion, Ag_8GeSe_6 still exhibits crystalline vibrational properties. Note, that the bulk of phonon modes persevere in the superionic phase, unveiling an inherent solid-like rather than liquid-like diffusion character. The applicability of the Chudley–Elliot jump diffusion model with an average jump distance and residence period is a consequence of the solid-like diffusion character.

Above all, these soft phonon modes do not only facilitate Ag diffusion but they enable a boosted scattering of acoustic phonons efficiently impeding thermal transport. In the superionic phase where the soft phonons are over-damped they are conjectured to induce diffuson-mediated thermal transport.[24] The diffuson-dominated thermal transport signifies a breakdown of phonon quasiparticles and its wavelike nature leading to thermal conductivities lower than the hypothetical glass limit as they have been reported in the literature.[23e,24]

Recent neutron scattering experiments on Cu_7PSe_6 Argyrodite have identified the largely anharmonic effects associated with the Cu-dominated low-frequency phonon modes and observed QENS signal of the mobile Cu atoms.[23e] They also observed that the vibrational modes associated with Cu contributions are strongly damped in the superionic phase, which corresponds to the breakdown of phonon quasiparticles.[23e] Recent Raman spectroscopy investigations on ionic conductors, such as AgI[25] and $Na_3P(S/Se)_4$,[26] have demonstrated the significant coupling between mobile ions and host lattice within the soft mode lattice instabilities. However, the core interconnection between soft phonon and atomic diffusion has not been well-established and elucidated in Ag-based Argyrodites. After the submission of our manuscript, we became aware of a similar study,[27] which is consistent with our results. In this study, we highlight Ag_8GeSe_6 as a show case to explicitly elucidate the interconnection between strongly damped soft phonons and mobile ions. Therefore, this exploration will establish an intertwined understanding to comprehend the connection between lattice and diffusive dynamics. It will also provide essential insights into the underlying mechanisms of macroscopic heat conduction and ion transport in superionic Argyrodites. We suggest that other Ag-based superionic Argyrodites might also hold these interesting features with similar interconnection between soft phonon and diffusive dynamics, and these compounds can be explored for further studies in the area of INS, QENS, Raman spectroscopy, and AIMD.

4. Experimental Section

Materials Synthesis: For the synthesis of the polycrystalline Ag_8GeSe_6 sample with an amount of 20 g, the melting-annealing method was utilized. The stoichiometric admixture of high-purity Ag (Shot, 99.999%), Ge (Shot, 99.999%), and Se (Shot, 99.999%) elements were weighted out, loaded into a cone-shaped sealed and evacuated (≈10^{-4} Pa) quartz tube. A homemade crystal-growth furnace was used for the sample synthesis. The quartz container was slowly heated to 1323 K over 24 h, followed by a dwelling at this temperature for 12 h. It was subsequently cooled to 873 K within 6 h and kept at this temperature for another 72 h. Finally, the sample was slowly cooled to room temperature over 72 h. The highly crystalline product was grounded into fine powders for the synchrotron and neutron experiments.

Synchrotron X-Ray Diffraction Characterization: *T*-dependent synchrotron X-ray diffraction experiments with a wavelength 0.7749 Å were

conducted on a powder sample of ≈1 mg from 250 to 600 K at the beamline of TPS09A at the National synchrotron radiation research center of Taiwan photon source (NSRRC). A cryostat was used to perform the low-temperature measurements from 250 to 350 K and utilized a heating furnace to conduct high-temperature measurements from 350 to 600 K. All synchrotron X-ray diffraction data were analyzed with the Rietveld method by using the GSAS (General Structure Analysis System)[28] and FullProf programs.

Inelastic Neutron Scattering Characterization: Inelastic neutron scattering and quasielastic neutron scattering experiments were performed on a powder sample of ≈10 g at temperatures between 2 and 600 K at the thermal neutron time-of-flight spectrometer PANTHER at the European Neutron Source Institut Laue Langevin in Grenoble, France.[29] The nominal incident energies E_i of 30 and 50 meV for the study of phonons and 12.5 meV for monitoring the low-energy phonon and QENS signal with a resolution of about 0.6 meV at the elastic line were applied. A standard cryostat was utilized for measurements at 2, 100, 200, and 300 K with the powder sample loaded in an aluminum sample holder. Acquisition periods varied between 1.5 and 3 h depending on E_i and temperature determining the inelastic intensity. Measurements between 300 and 600 K were carried out in a high-temperature furnace with the sample loaded in a niobium sample holder. Data were recorded for 1.5 and 2 h at 300, 400, 500, and 600 K. The temperature evolution of the QENS signal in the regime of multiple phase transitions was carried out upon cooling from 500 K to room temperature with E_i = 12.5 meV. An acquisition period of 10 min resulted in a temperature difference between spectra of 5 K and less. Ancillary measurements of empty sample holders, sample environments and vanadium were carried out for a standardized data correction procedure and conversion of the corrected signal to the dynamic structure factor $S(|\boldsymbol{Q}|, E)$ and generalized density of states $G(E)$. The Mantid software package was applied for the correction and conversion computing.[30] Spectra at constant momentum transfers $|\boldsymbol{Q}|$ = 0.8–1.4 and 2.88 Å^{-1} were extracted at various temperatures from $S(|\boldsymbol{Q}|, E)$ with a $|\boldsymbol{Q}|$ bin of 0.25 Å^{-1}. The resolution was determined from low-$|\boldsymbol{Q}|$ scattering at T = 300 K in the absence of QENS (black line in Figure 6a).

Computational Methods: Input configurations for the temperature-dependent effective potential (TDEP) of the orthorhombic phase of Ag_8GeSe_6 were generated by AIMD on a 2 × 2 × 2 supercell comprising 240 atoms at 300 K. Nonspin polarized density functional theory (DFT) calculations were performed using the projector augmented wave (PAW)[31] method as implemented in the Vienna ab initio simulation package (VASP).[32] The PBE functional[33] of generalized gradient approximation (GGA) was applied as the exchange-correlation functional. An energy convergence criterion of 1 × 10^{-8} eV and a plane wave energy cutoff of 500 eV were used during the self-consistent electronic calculations. To accurately calculate the atomic forces, a Monkhorst–Pack k-mesh[34] of 2 × 2 × 2 was used to sample the Brillouin-zone of the 240-atom supercell. The renormalized second-order force constants were extracted using the TDEP scheme as implemented in hiPhive.[35] The cutoff distances for the second- and third-order terms were set to 9.0 and 5.0 Å, respectively. The root mean square error (RMSE) of the fitted forces was below 0.094 meV Å^{-1}.

To simulate the partial occupation of lattice sites of Ag atoms in the cubic phase of Ag_8GeSe_6, AIMD simulations were performed on a 240-atom supercell at a temperature range of 300–600 K. A Γ point mesh combined with an energy convergence of 10^{-3} eV was applied to the AIMD simulations. The duration of AIMD simulations was 200 ps with a 5 fs time step. The orthorhombic structure of Ag_8GeSe_6 obtained from X-ray diffraction refinement was applied as the initial configuration of the AIMD simulations at 300 K. The partial occupancy of Ag atoms in the high-temperature cubic phase of Ag_8GeSe_6 was simulated by mixing 32 Ag atoms with 88 vacancies (120 Ag partial occupation lattice sites) with the special quasi-random structure (SQS) algorithm[36] as shown in (Figure S6, Supporting Information). The SQS structure was used as the initial configuration of AIMD simulations of the cubic phase at 400, 500, and 600 K. PDOS were obtained by calculating the Fourier transform of the velocity autocorrelation function based on AIMD simulations under the *NVT* ensemble at 300, 400, 500, and 600 K. Before data collection, all systems were initially equilibrated for at least 10 ps under the *NVT* ensemble with Nose–Hoover thermostat. The mean square displacement (MSD) was calculated using

$$MSD\ (t) = \frac{\sum_{i=1}^{N} (r_i(t) - r_i(t_0))^2}{N} \quad (4)$$

where N is the number of atoms and $r_i(t)$ is the position of atom i at time t.

Neutron Spectroscopy Simulations: Simulations of neutron scattering intensities based on AIMD simulations were performed via MDANSE[21] software based on the initial input file of trajectory from AIMD simulation.[29] The trajectory provides the detailed information of the atomic motions by tracing the atomic coordinates at specified time intervals, and enables us to investigate properties of the static structure and lattice dynamics behavior captured in the dynamic structure factor $S(|\boldsymbol{Q}|, E)$. Importantly, the measured $S(|\boldsymbol{Q}|, E)$ consists of a coherent and an incoherent part

$$S\ (|\mathbf{Q}|, E) = S_{\text{coh}}\ (|\mathbf{Q}|, E) + S_{\text{inc}}\ (|\mathbf{Q}|, E) \quad (5)$$

While our experiment cannot discriminate between the two contributions, simulations via MDANSE can easily simulate the total $S(|\boldsymbol{Q}|, E)$ or only $S_{\text{inc}}(|\boldsymbol{Q}|, E)$ or $S_{\text{coh}}(|\boldsymbol{Q}|, E)$.

Supporting Information

Supporting Information is available from the Wiley Online Library or from the author.

Acknowledgements

X.S. acknowledged the Helmholtz-OCPC Postdoc Program (No. ZD202029). X.S. acknowledged funding from the European Union's Horizon 2020 research and innovation program under the Marie Sklodowska-Curie Grant Agreement No. 101034329. X.S. acknowledged the WINNINGNormandy Program supported by the Normandy Region. X.S., M.M.K., and F.W. acknowledged the European Neutron Source Institut Laue Langevin (ILL), Grenoble, France for the provision of neutron beamtime of the proposal (No. 7-01-541) at beamline Panther. X.S., Y.-H.T., and C.-C.Y. acknowledged the National synchrotron radiation research center Taiwan photon source (NSRRC), Taiwan for the provision of synchrotron radiation of our proposals (Nos. 2020-2-105-1, 2021-2-093-1, and 2022-1-139-1) at the beamline of TPS09A. C.-C.Y. and Y.-H.T. acknowledged the financial support from the Ministry of Science and Technology of Taiwan, under the Grant Nos. 111-2112-M-0080934 and 110-2112-M-033-011. N.O., C.W., and Y.C. are grateful for the research computing facilities offered by ITS, HKU.

Open access funding enabled and organized by Projekt DEAL.

Conflict of Interest

The authors declare no conflict of interest.

Data Availability Statement

The data that support the findings of this study are openly available in Institut Laue-Langevin at https://doi.org/10.5291/ILL-DATA.7-01-541, reference number 701541.

Keywords

fast diffusion, neutron scattering, soft phonons, superionic argyrodites, thermoelectrics

Received: June 15, 2023
Revised: July 30, 2023
Published online:

[1] a) E. Bell Lon, *Science* **2008**, *321*, 1457; b) D. G. Onn, A. Witek, Y. Z. Qiu, T. R. Anthony, W. F. Banholzer, *Phys. Rev. Lett.* **1992**, *68*, 2806; c) J. He, T. M. Tritt, *Science* **2017**, *357*, eaak9997; d) T. Zhu, Y. Liu, C. Fu, J. P. Heremans, J. G. Snyder, X. Zhao, *Adv. Mater.* **2017**, *29*, 1605884; e) T. Li, J. Song, X. Zhao, Z. Yang, G. Pastel, S. Xu, C. Jia, J. Dai, C. Chen, A. Gong, F. Jiang, Y. Yao, T. Fan, B. Yang, L. Wågberg, R. Yang, L. Hu, *Sci. Adv.* **2018**, *4*, eaar3724; f) P. Padture Nitin, M. Gell, H. Jordan Eric, *Science* **2002**, *296*, 280.

[2] a) T. Ghosh, M. Dutta, D. Sarkar, K. Biswas, *J. Am. Chem. Soc.* **2022**, *144*, 10099; b) C. Chang, L.-D. Zhao, *Mater. Today Phys.* **2018**, *4*, 50.

[3] a) C. W. Li, O. Hellman, J. Ma, A. F. May, H. B. Cao, X. Chen, A. D. Christianson, G. Ehlers, D. J. Singh, B. C. Sales, O. Delaire, *Phys. Rev. Lett.* **2014**, *112*, 175501; b) O. Delaire, J. Ma, K. Marty, A. F. May, M. A. McGuire, M. H. Du, D. J. Singh, A. Podlesnyak, G. Ehlers, M. D. Lumsden, B. C. Sales, *Nat. Mater.* **2011**, *10*, 614; c) C. W. Li, J. Hong, A. F. May, D. Bansal, S. Chi, T. Hong, G. Ehlers, O. Delaire, *Nat. Phys.* **2015**, *11*, 1063.

[4] a) R. A. Cowley, S. M. Shapiro, *J. Phys. Soc. Jpn.* **2006**, *75*, 111001; b) R. A. Cowley, S. N. Gvasaliya, S. G. Lushnikov, B. Roessli, G. M. Rotaru, *Adv. Phys.* **2011**, *60*, 229.

[5] G. Shirane, Y. Yamada, *Phys. Rev.* **1969**, *177*, 858.

[6] S. Ohno, A. Banik, G. F. Dewald, M. A. Kraft, T. Krauskopf, N. Minafra, P. Till, M. Weiss, W. G. Zeier, *Prog. Energy* **2020**, *2*, 022001.

[7] N. Q. Minh, *J. Am. Ceram. Soc.* **1993**, *76*, 563.

[8] a) K. Zhao, P. Qiu, X. Shi, L. Chen, *Adv. Funct. Mater.* **2020**, *30*, 1903867; b) S. Lin, W. Li, Y. Pei, *Mater. Today* **2021**, *48*, 198.

[9] a) H. L. Liu, X. Shi, F. F. Xu, L. L. Zhang, W. Q. Zhang, L. D. Chen, Q. Li, C. Uher, T. Day, G. J. Snyder, *Nat. Mater.* **2012**, *11*, 422; b) Z. Zhang, K. Zhao, T.-R. Wei, P. Qiu, L. Chen, X. Shi, *Environ. Sci.* **2020**, *13*, 3307.

[10] a) B. Li, H. Wang, Y. Kawakita, Q. Zhang, M. Feygenson, H. L. Yu, D. Wu, K. Ohara, T. Kikuchi, K. Shibata, T. Yamada, X. K. Ning, Y. Chen, J. Q. He, D. Vaknin, R. Q. Wu, K. Nakajima, M. G. Kanatzidis, *Nat. Mater.* **2018**, *17*, 226; b) S. Bhattacharya, R. Basu, R. Bhatt, S. Pitale, A. Singh, D. K. Aswal, S. K. Gupta, M. Navaneethan, Y. Hayakawa, *J. Mater. Chem. A* **2013**, *1*, 11289.

[11] S. Lin, W. Li, S. Li, X. Zhang, Z. Chen, Y. Xu, Y. Chen, Y. Pei, *Joule* **2017**, *1*, 816.

[12] W. Li, S. Lin, B. Ge, J. Yang, W. Zhang, Y. Pei, *Adv. Sci.* **2016**, *3*, 1600196.

[13] K. S. Weldert, W. G. Zeier, T. W. Day, M. Panthöfer, G. J. Snyder, W. Tremel, *J. Am. Chem. Soc.* **2014**, *136*, 12035.

[14] a) J.-Y. Liu, L. Chen, L.-M. Wu, *Nat. Commun.* **2022**, *13*, 2966; b) A. Charoenphakdee, K. Kurosaki, H. Muta, M. Uno, S. Yamanaka, *Phys. Status Solidi RRL* **2008**, *2*, 65; c) A. Charoenphakdee, K. Kurosaki, H. Muta, M. Uno, S. Yamanaka, *Jpn. J. Appl. Phys.* **2009**, *48*, 011603; d) B. B. Jiang, P. F. Qiu, E. Eikeland, H. Y. Chen, Q. F. Song, D. Ren, T. S. Zhang, J. Yang, B. B. Iversen, X. Shi, L. D. Chen, *J. Mater. Chem. C* **2017**, *5*, 943; e) X. Shen, Y. Xia, C.-C. Yang, Z. Zhang, S. Li, Y.-H. Tung, A. Benton, X. Zhang, X. Lu, G. Wang, J. He, X. Zhou, *Adv. Funct. Mater.* **2020**, *30*, 2000526.

[15] W. F. Kuhs, R. Nitsche, K. Scheunemann, *Mater. Res. Bull.* **1979**, *14*, 241.

[16] F. Boucher, M. Evain, R. Brec, *J. Solid State Chem.* **1993**, *107*, 332.

[17] X. Shen, C.-C. Yang, Y. Liu, G. Wang, H. Tan, Y.-H. Tung, G. Wang, X. Lu, J. He, X. Zhou, *ACS Appl. Mater. Interfaces* **2019**, *11*, 2168.

[18] B. Fåk, B. Dorner, *Physica B+C* **1997**, *234-236*, 1107.

[19] W. Cochran, *Adv. Phys.* **1960**, *9*, 387.

[20] a) F. Weber, R. Hott, R. Heid, K. P. Bohnen, S. Rosenkranz, J. P. Castellan, R. Osborn, A. H. Said, B. M. Leu, D. Reznik, *Phys. Rev. B* **2013**, *87*, 245111; b) M. Maschek, S. Rosenkranz, R. Hott, R. Heid, M. Merz, D. A. Zocco, A. H. Said, A. Alatas, G. Karapetrov, S. Zhu, J. van Wezel, F. Weber, *Phys. Rev. B* **2016**, *94*, 214507.

[21] G. Goret, B. Aoun, E. Pellegrini, *J. Chem. Inf. Model.* **2017**, *57*, 1.

[22] C. T. Chudley, R. J. Elliott, *Proc. Phys. Soc.* **1961**, *77*, 353.

[23] a) S. M. K. Nazrul Islam, P. Mayank, Y. Ouyang, J. Chen, A. K. Sagotra, M. Li, M. B. Cortie, R. Mole, C. Cazorla, D. Yu, X. Wang, R. A. Robinson, D. L. Cortie, *Acta Mater.* **2021**, *215*, 117026; b) J. Ding, L. Niedziela Jennifer, D. Bansal, J. Wang, X. He, F. May Andrew, G. Ehlers, L. Abernathy Douglas, A. Said, A. Alatas, Y. Ren, G. Arya, O. Delaire, *Proc. Natl. Acad. Sci. USA* **2020**, *117*, 3930; c) J. L. Niedziela, D. Bansal, A. F. May, J. Ding, T. Lanigan-Atkins, G. Ehlers, D. L. Abernathy, A. Said, O. Delaire, *Nat. Phys.* **2019**, *15*, 73; d) M. K. Gupta, J. Ding, N. C. Osti, D. L. Abernathy, W. Arnold, H. Wang, Z. Hood, O. Delaire, *Environ. Sci.* **2021**, *14*, 6554; e) M. K. Gupta, J. Ding, D. Bansal, D. L. Abernathy, G. Ehlers, N. C. Osti, W. G. Zeier, O. Delaire, *Adv. Energy Mater.* **2022**, *12*, 2200596; f) D. J. Voneshen, H. C. Walker, K. Refson, J. P. Goff, *Phys. Rev. Lett.* **2017**, *118*, 145901; g) A. J. E. Rettie, J. Ding, X. Zhou, M. J. Johnson, C. D. Malliakas, N. C. Osti, D. Y. Chung, R. Osborn, O. Delaire, S. Rosenkranz, M. G. Kanatzidis, *Nat. Mater.* **2021**, *20*, 1683.

[24] T. Bernges, R. Hanus, B. Wankmiller, K. Imasato, S. Lin, M. Ghidiu, M. Gerlitz, M. Peterlechner, S. Graham, G. Hautier, Y. Pei, M. R. Hansen, G. Wilde, G. J. Snyder, J. George, M. T. Agne, W. G. Zeier, *Adv. Energy Mater.* **2022**, *12*, 2200717.

[25] T. M. Brenner, C. Gehrmann, R. Korobko, T. Livneh, D. A. Egger, O. Yaffe, *Phys. Rev. Mater.* **2020**, *4*, 115402.

[26] T. M. Brenner, M. Grumet, P. Till, M. Asher, W. G. Zeier, D. A. Egger, O. Yaffe, *J. Phys. Chem. Lett.* **2022**, *13*, 5938.

[27] Q. Ren, M. K. Gupta, M. Jin, J. Ding, J. Wu, Z. Chen, S. Lin, O. Fabelo, J. A. Rodríguez-Velamazán, M. Kofu, K. Nakajima, M. Wolf, F. Zhu, J. Wang, Z. Cheng, G. Wang, X. Tong, Y. Pei, O. Delaire, J. Ma, *Nat. Mater.* **2023**, *22*, 999.

[28] B. Toby, *J. Appl. Crystallogr.* **2001**, *34*, 210.

[29] X. Shen, B. Fak, M. Koza, F. Weber, Lattice dynamics in liquid-like thermoelectric material Ag_8GeSe_6. Institut Laue-Langevin (ILL). https://doi.org/10.5291/ILL-DATA.7-01-541 (accessed: August 2021).

[30] O. Arnold, J. C. Bilheux, J. M. Borreguero, A. Buts, S. I. Campbell, L. Chapon, M. Doucet, N. Draper, R. Ferraz Leal, M. A. Gigg, V. E. Lynch, A. Markvardsen, D. J. Mikkelson, R. L. Mikkelson, R. Miller, K. Palmen, P. Parker, G. Passos, T. G. Perring, P. F. Peterson, S. Ren, M. A. Reuter, A. T. Savici, J. W. Taylor, R. J. Taylor, R. Tolchenov, W. Zhou, J. Zikovsky, *Nucl. Instrum. Methods Phys. Res., Sect. A* **2014**, *764*, 156.

[31] G. Kresse, J. Furthmüller, *Phys. Rev. B* **1996**, *54*, 11169.

[32] G. Kresse, J. Hafner, *Phys. Rev. B* **1993**, *47*, 558.

[33] G. K. Madsen, *Phys. Rev. B* **2007**, *75*, 195108.

[34] H. J. Monkhorst, J. D. Pack, *Phys. Rev. B* **1976**, *13*, 5188.

[35] F. Eriksson, E. Fransson, P. Erhart, *Adv. Theory Simul.* **2019**, *2*, 1800184.

[36] A. Van De Walle, *Calphad* **2009**, *33*, 266.